Capsule distributions and flow properties in curved tubes

Huiyong Feng,[1] Jianguo Zheng,[2] Bei Wei,[3,4] Jian Hou,[3,4] and Haibo Huang[1,*]
[1]*Department of Modern Mechanics, University of Science and Technology of China, Hefei, Anhui 230026, People's Republic of China*
[2]*School of Aerospace Engineering, Huazhong University of Science and Technology, Wuhan, Hubei 430074, People's Republic of China*
[3]*Key Laboratory of Unconventional Oil & Gas Development (China University of Petroleum (East China)), Ministry of Education, Qingdao 266580, People's Republic of China*
[4]*School of Petroleum Engineering, China University of Petroleum (East China), Qingdao 266580, People's Republic of China*

(Received 7 June 2022; accepted 17 January 2023; published 31 January 2023)

The distribution of capsules and rheological properties of suspensions in curved tubes are investigated by using an immersed-boundary lattice Boltzmann method. We mainly focus on the effective suspension viscosity and equilibrium positions of capsules as functions of Reynolds number (Re), Capillary number (Ca) and volume fraction of capsules (ϕ). We found that at limited inertia (Re $O(10)$), the effective viscosity decreases with increasing Re, which is different from the variation trend in straight tubes. Dean's vortices play an important role. When the fluid inertia increases, the vortices are strengthened. They greatly promote the capsules' circumferential transportation by trapping the capsules into their centers and making the location of maximum azimuthal velocity close to them. The curvature effect of the torus vessel is also investigated. When the curvature κ is large enough, e.g., $\kappa > 0.2$, a scaling law for the effective viscosity as a function of a redefined Re is proposed. Furthermore, the distribution feature of multiple capsules in the torus vessel is revealed. Generally, for the semidilute regime, the capsules concentrate on the symmetrical plane at low Re but the center of Dean's vortex at high Re. In addition, for both the dilute and semidilute regime, the scaling law connecting the effective viscosity and the average location of capsules is proposed. Our data support the scaling well. This study may be useful in the design of tubes for capsule transportation.

DOI: 10.1103/PhysRevFluids.8.013604

I. INTRODUCTION

Transportation of capsule suspensions in curved tubes is an important problem in physiology and microfluidics. In many situations, capsule suspensions flow through a complicated network of tubes or curved channels, such as red blood cells transport in the human circulation and artificial capsules flow through microfluidic devices. In physiology, many blood diseases are usually accompanied by the curvature of blood vessels [1]. For example, atherosclerosis tends to occur in areas where these vessels bend and branch [2–5]. In microfluidics, curved tubes are often used for cell or capsule separation and aggregation. Several studies used unlabeled helical microfluidics to isolate circulating tumor cells from other normal cells [6–8]. Moreover, many experiments about the tube's curvature effect on the separation of particles of different sizes have been carried out. Kutaegowdanahalli *et al.* [9–11] first used spiral tubes for sorting microparticles with efficiency

*http://staff.ustc.edu.cn/~huanghb; huanghb@ustc.edu.cn

 ©2023 American Physical Society

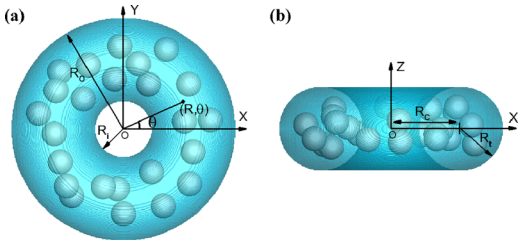

FIG. 1. Geometry for a torus vessel, (a) top view, (b) side view. The tube's radius is R_t. Here R_i and R_o are the radii of the inner and outer walls, respectively. $Z = 0$ denotes the symmetrical plane. Curvature radius R_c is defined as the distance between the origin O and the vessel's centerline.

over 80%. Russom *et al.* [12] used a similar device with a low channel aspect ratio to separate microparticles and found that the focusing behavior was not affected by particle density. After these, there are many other similar separation experiments [13–15]. Besides the spiral tubes, the serpentine tubes (another type of curved tubes) are also used to separate microparticles by Di Carlo *et al.* [16]. It is necessary to further understand the flow properties in curved tubes.

In curved tubes, the flow undergoes outward centrifugal acceleration and forms secondary flow: a pair of counter-rotating vortices, i.e., Dean's vortices. Dean's vortices are first analyzed with the perturbation method in torus vessels by Dean [17]. The geometry of a torus vessel is shown in Fig 1. It is a spiral tube with zero spiral pitch. Because this kind of curved tube is simple and the curvature is uniform, numerous studies on the single-phase flow in the tube have been performed. Barua *et al.* [18–21] discussed the secondary flows of the circular cross section in torus vessels under different Dean numbers theoretically and numerically. Cheng *et al.* [22–24] obtained the velocity distribution in the torus vessels with triangular and rectangular cross sections through numerical calculation. Siggers and Waters [25] performed a comprehensive analysis and gave qualitative features of steady curved-tube flows.

In our study, torus vessels are adapted. For suspension flow in torus vessel, the capsules can reach an equilibrium state quickly. In reality, how to drive the flow inside the torus may be a technical issue. On the other hand, the flow inside an infinite spiral tubes with small spiral pitch p should be similar to that inside our torus vessels; this has been considered in previous work. [26]. In other words, if the flow in extending direction (z direction in Fig. 1) can be ignored, the flow in one coil of a spiral tube with periodic boundary on its inlet/outlet circular cross sections should be close to that inside our torus vessel.

For suspension flows in straight tubes, there are a large number of studies on the dynamics of either single-capsule suspensions [27–31] or multicapsule suspensions [32–36]. However, there are few studies, especially numerical studies, on the capsule suspension in curved tubes. Ye *et al.* [37,38] studied the movement and deformation of a single Red Blood Cell (RBC) in various curved tubes, e.g., spiral tube or U-shaped tube, and found that Dean's vortex can greatly affect the deformation of the capsules. Balogh and Bagchi [34,39] analyzed the cell-free-layer (CFL) profiles in microvascular networks within vivolike topologies. They showed that the vessel tortuosity causes the CFL to become more asymmetric along with the flow. Ebrahimi *et al.* [40,41] did comprehensive studies on the migration and deformation of a single capsule in torus vessels of circular and rectangular cross sections. However, in blood flows or industrial flows, e.g., the flow of coal water slurry, usually macroscopic viscosity of the suspension is more important and useful [33,42,43]. Here, we focus on the influence of the Dean's vortex on the apparent viscosity of the suspension. The ultimate goal is to understand the rheology of capsule suspensions and the distribution of capsules in curved tubes.

Inertia is an important factor that would affect the migration of rigid particles and deformable capsules. When inertia is present, particles can undergo cross-stream migration, and finally settle at an equilibrium radial position away from the tube center. For rigid particles, the equilibrium position is 0.6 times the tube radius from the tube center which was reported by Segré and Silberberg [44]

(Segré-Silberberg effect). Then Matas *et al.* [45–47] analyzed the shift of equilibrium position of rigid particles theoretically and experimentally. They found that depending on Re (the character length scale is the diameter of the tube, which is also applicable to the following Re in this paragraph), rigid particles are mainly distributed at two positions: Segré-Silberberg annulus and inner annulus. Different from rigid particles, the equilibrium position of soft capsules changes continuously with Re. The equilibrium position is off centered at low to medium Re, but shifts toward the centerline at high Re [32,33,35]. Inertia also plays an important role when curvatures are considered. Majji and Morris [48] found three regimes of particle distribution in Taylor-Couette flows at different Re. For curved tube flows, as the fluid inertia increases, the Dean's vortex becomes stronger. It can be quantified by a dimensionless number, i.e., Dean number $\mathrm{De} = \mathrm{Re}\sqrt{\frac{D_h}{2R}}$, where D_h is the tube diameter, R is the radius of curvature [36]. When the size of curved tubes is fixed, De can be represented by Re. According to Ref. [40], when Re is small, the capsule stays on the symmetrical plane, while at high Re, it would move to the center of the vortex. This behavior can significantly affect the rheology of suspensions. In this paper, we mainly focus on the fluid inertia effect. Besides, the rheology properties and the distribution of multiple capsules under various κ and ϕ in curved tubes are also explored.

To the best of our knowledge, there is so far no systematic and in-depth three-dimensional numerical study on the rheology and distribution of deformable capsules in the curved tubes. The change of effective viscosity with Re and κ, as well as the distribution of multiple capsules in curved tubes remains unclear. In this paper, not only the dilute regime with one single capsule but also the semidilute regime with multiple capsules are studied. The spatial distribution of capsules and the apparent viscosity of suspension in both curved and straight tubes are compared and analyzed. The role of Dean's vortex is analyzed in detail.

The article is organized as follows. In Sec. II, the problem description, membrane model, and numerical method are introduced and validated. The results of single-capsule and multiple-capsule suspensions in torus vessels are presented in Sec. III. Conclusions are in Sec. IV.

II. PROBLEM STATEMENT

The equation of the torus vessel is $Z^2 = R_t^2 - (R_c - \sqrt{(X^2 + Y^2)})^2$. Both the Cartesian coordinates (X, Y, Z) and the cylindrical coodinates (R, θ, Z) are shown in Fig 1. The curvature radius R_c and tube radius R_t are defined in the caption of Fig 1. In our simulations, the fluid in the torus is driven by a body force or an azimuthal pressure gradient $\frac{1}{R_c}\frac{dp}{d\theta} = -4\mu_0 U_0/R_t^2$ [40], where μ_0 is the viscosity of the fluid and U_0 is the maximum velocity in a straight tube with radius R_t if pressure gradient along the flow $\frac{dp}{dx} = \frac{1}{R_c}\frac{dp}{d\theta}$ is applied.

A. Methodology

In numerical simulations, each capsule is modeled as a liquid drop covered by a two-dimensional (zero-thickness) hyperelastic membrane. The membrane density is the same as the fluid. Also the mechanical properties of the fluid inside and outside of the capsule are identical. To simulate the migration and deformation of capsules, the capsule surface is discretized into thousands of triangular elements [49]. The force of the Lagrangian nodes of the triangular elements is obtained by solving the constitutive equation. Skalak's (SK) law [50], which can model the shear deformation and area dilation of membrane is used

$$W^{\mathrm{SK}} = \tfrac{1}{4}G_s\left(I_1^2 + 2I_1 - 2I_2\right) + \tfrac{1}{4}CG_sI_2^2, \tag{1}$$

where W is the strain energy density per unit membrane area. G_s is the surface shear modulus, C is the volume modulus ratio. I_1, I_2 are the first and second strain invariants with $I_1 = \lambda_1^2 + \lambda_2^2 - 2$ and $I_2 = (\lambda_1\lambda_2)^2 - 1$. λ_1 and λ_2 are the principal extension ratios in the plane of the membrane. For biological membranes, C must be large enough to ensure negligible area dilation. However for artificial capsules, taking a large value of C would cause numerical instability and lead to no

deformation. Therefore in the present study, C is set to be 10, which is identical to that in Ref. [40]. This value would not lead to numerical instability and can provide a large deformation.

The tensile forces acting on the Lagragian nodes are obtained from the strain energy function W using the principal virtual work as

$$\boldsymbol{f}_t(\boldsymbol{s}) = -\frac{\partial W}{\partial \boldsymbol{v}}, \tag{2}$$

where $\boldsymbol{v}$ is the displacement of the Lagragian node $\boldsymbol{s}$ on the capsule membrane.

The bending resistance of the membrane is modeled as a force density [51]:

$$\boldsymbol{f}_b = k_b\big[(2k_m + c_0)\big(2k_m^2 - 2k_g - c_0 k_m\big) + 2\Delta_{\mathrm{LB}} k_m\big]\boldsymbol{n}, \tag{3}$$

where k_m, k_g, c_0 are the mean, Gaussian, and spontaneous curvatures, respectively. Δ_{LB} is the Laplace-Beltrami operator and $\boldsymbol{n}$ is the unit normal vector. Finally, the total force of the Lagragian node on the membrane is the sum of the tensile force $\boldsymbol{f}_t$ parallel to the membrane surface and the bending force $\boldsymbol{f}_b$ perpendicular to the membrane surface, $\boldsymbol{f}_m = \boldsymbol{f}_t + \boldsymbol{f}_b$.

The fluid flow is simulated using the lattice Boltzmann method (LBM) [52]. The LBM originates from lattice gas automata. Macroscopically, it is able to recover the incompressible Navier-Stokes equations. The discretized lattice Boltzmann equation is

$$f_i(\boldsymbol{x} + c_i\Delta t, t + \Delta t) - f_i(\boldsymbol{x}, t) = \frac{1}{\tau}(f_i(\boldsymbol{x}, t) - f_i^{\mathrm{eq}}(\boldsymbol{x}, t)) + \Delta t S_i, \tag{4}$$

where $f_i(\boldsymbol{x}, t)$ is the distribution function at time t and position $\boldsymbol{x}$. Here $D3Q19$ velocity model is adopted [53] and c_i is the ith discrete velocity, where $i = 0..., 18$. Here Δt is time step and τ is the relaxation time, which is related to the dynamic viscosity in the NS equation $\mu = \rho c_s^2(\tau - 0.5)\Delta t$. The equilibrium distribution function $f_i^{\mathrm{eq}}(\boldsymbol{x}, t)$ adopts the form

$$f_i^{\mathrm{eq}}(\boldsymbol{x}, t) = \omega_i \rho\left[1 + \frac{\boldsymbol{e_i}\cdot\boldsymbol{u}}{c_s^2} + \frac{(\boldsymbol{e_i}\cdot\boldsymbol{u})^2}{2c_s^4} - \frac{(\boldsymbol{u})^2}{2c_s^2}\right], \tag{5}$$

where the weighting coefficients are $\omega_0 = 1/3$, $\omega_i = 1/18$ $(i = 1 - 6)$ and $\omega_i = 1/36$ $(i = 7 - 18)$. The lattice sound speed $c_s = \Delta x/(\sqrt{3}\Delta t)$. The source term in the lattice Boltzmann equation is

$$S_i = \left(1 - \frac{1}{2\tau}\right)\omega_i\left[\frac{\boldsymbol{e_i} - \boldsymbol{u}}{c_s^2} + \frac{\boldsymbol{e_i}\cdot\boldsymbol{u}}{c_s^4}\boldsymbol{e_i}\right]\boldsymbol{F}. \tag{6}$$

The macroscopic quantities of the fluid, such as density, velocity, and pressure can be calculated from the distribution function as

$$\rho = \sum_i f_i, \quad \boldsymbol{u} = \frac{1}{\rho}\sum_i f_i \boldsymbol{e_i} + \frac{1}{2\rho}\boldsymbol{F}\Delta t, \quad p = c_s^2\rho. \tag{7}$$

The coupling between the solid and fluid is achieved by the immersed boundary method (IBM) [54] to ensure the nonslip boundary condition. In the implementation of the IBM, first the fluid velocity at the Lagrangian node $\boldsymbol{s}$ on the capsule surface is interpolated from the velocities of surrounding fluid nodes, i.e.,

$$\boldsymbol{u}(\boldsymbol{s}) = \int_V \delta(\boldsymbol{x} - \boldsymbol{s})\boldsymbol{u}(\boldsymbol{x})dV, \tag{8}$$

where $\boldsymbol{s}$ and $\boldsymbol{x}$ are the locations of Lagrangian points and fluid nodes, respectively. V represents the fluid domain. δ is the delta function

$$\delta(\boldsymbol{x} - \boldsymbol{s}) = \delta(x - x(\boldsymbol{s}))\delta(y - y(\boldsymbol{s}))\delta(z - z(\boldsymbol{s})), \tag{9}$$

where

$$\delta(r) = \begin{cases} \frac{1}{4}\left(1 + \cos\left(\frac{\pi|r|}{2}\right)\right), & |r| \leqslant 2 \\ 0, & |r| > 2. \end{cases} \tag{10}$$

Then, according to Newton's second law, Lagrangian points may move $\boldsymbol{u}(\boldsymbol{s})\Delta t$. Due to the displacement or deformation, the force $\boldsymbol{f}_m$ acting on the Lagrangian point can be calculated through constitutive law and bending equation. Finally, $\boldsymbol{f}_m$ has to be spread to the surrounding fluid nodes through

$$\boldsymbol{F}(\boldsymbol{x}) = \int_V \delta(\boldsymbol{x} - \boldsymbol{s})\boldsymbol{f}_m(\boldsymbol{s})dV. \tag{11}$$

It is noted that this force should be added to the lattice Boltzmann equation as an external force.

The problem depends on several dimensionless parameters. The tube Reynolds number $\mathrm{Re} = (\rho U_0 R_t)/\mu_0$. The capillary number $Ca = (\mu_0 U_0)/G_s$ where G_s is the surface shear modulus. Ca measures the ratio between the viscous and elastic forces. The dimensionless bending stiffness $E_b = k_b/(G_s a^2)$ where k_b is the bending modulus, a is the radius of capsule. E_b measures the relative importance of the membrane bending to shear elastic effects. Unless otherwise specified, E_b is kept at a constant 0.01, mainly to prevent the formation of membrane wrinkles [55]. The volume fraction of capsules $\phi = \frac{\frac{4}{3}\pi a^3}{2\pi R_c \cdot \pi R_t^2}$. The curvature of the torus vessel is defined as $\kappa = R_t/R_c$. The smaller the curvature is, the less bending the tube is. When the curvature approaches 0, the tube is straight. Unless otherwise specified, in the following descriptions, lengths, velocities, and time are normalized by a, U_0, a/U_0, respectively. For the polymeric capsules in linear flows, many studies focus on the deformation and inclination of capsules with a size of $0.03 \sim 2$ mm. Usually, the viscosity of the fluid is $0.1 \sim 1$ Pa s and channel width is $5 \sim 80$ times the radius of capsules [56–59]. For the experimental feasibility of our typical cases, according to the above common choices, suppose $a \sim 0.03$ mm, $\mu_0 \sim 0.1$ Pa · s, through calculations of nondimensional parameters, the properties of capsules should be $G_s = 1\times10^{-3} \sim 10$ N/m, $E_b \sim 10^{-11}$ N m.

B. Validation

We first simulate the motion and deformation of a large spherical capsule in a long straight tube with square cross section. In the simulations, tube length is 18, mesh resolution $\Delta x = 0.04$. The radius ratio between the capsule and the tube is $a/R_t = 0.85$. The three-dimensional capsule is discretized into 8192 triangular elements and 4098 Lagrangian nodes. The equilibrium deformed profiles are plotted in Fig 2. It can be seen that our equilibrium profiles agree well with that in the literature [60]. Second, the flow without capsules in a torus is simulated. For the fully developed flow without inertia in the tours vessel, the analytical solution of azimuthal velocity U is given by the well-known Dean's solution [17]:

$$U/U_0 = (1 - r^2) - \frac{3\kappa}{4} r(1 - r^2)\cos\theta + \frac{\kappa^2}{32}(1 - r^2)(-3 + 11r^2 + 10r^2\cos 2\theta) + O(\kappa^3), \tag{12}$$

where $r = R/R_t$ represents the radial position, (R, θ) are the polar coordinates defined in Fig 1. The first term on the right-hand side of the equation represents the velocity profile of Poiseuille flow in a straight tube, while the remaining terms represent the curvature effect. Figure 3(a) shows the contours of U. The contours are symmetric about the dashed line (the symmetrical plane $Z = 0$) but they are not left-right symmetric. The location of the maximum velocity U_m, i.e., R'_{U_m} occurs in the symmetrical line but is closer to the inner wall, see Fig. 3(b). The location is a function of κ [40]:

$$R'_{U_m} = -\frac{3\kappa}{8} + O(\kappa^3), \tag{13}$$

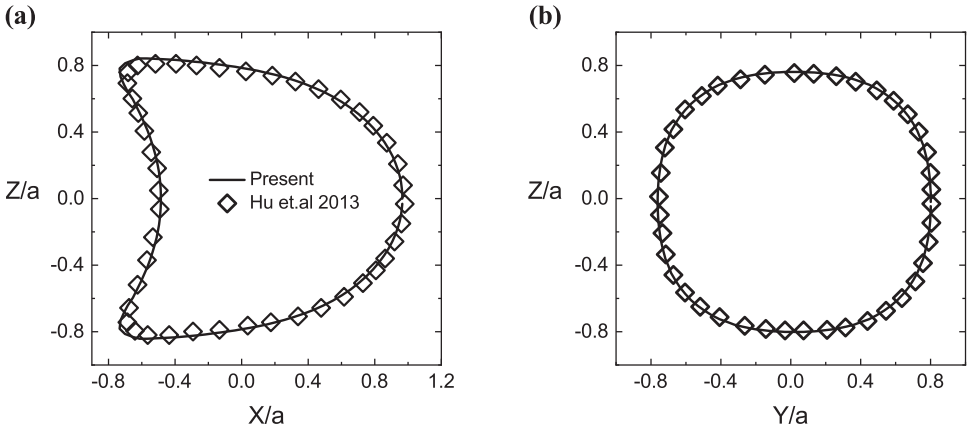

FIG. 2. Equilibrium profiles of an initially spherical capsule with SK membrane (Re $= 0.125$, $E_b = 0$, Ca $= 0.1$, $C = 1$) in a square section channel. (a) Profile in the XZ plane, (b) Cross profile in the YZ plane. The solid lines represent our results. The diamond symbols denote the results obtained by Hu *et al.* [60] using boundary element method.

where R' is the normalized radial location along the symmetrical plane, which is defined as $R' = \frac{R-R_c}{R_t}$. It is noted that $R' = -1, 0, 1$ represent the innermost edge of the vessel on the plane of $Z = 0$, vessel centerline, and the outermost edge on the plane, respectively. The negative sign in the above equation indicates that R'_{U_m} is closer to the inner wall. As the curvature increases, R'_{U_m} further moves towards the inner wall. Figure 3(c) shows R'_{U_m} as a function of κ. In the cases, $R_t = 2a$ and Re $=$ 0.05 are fixed but the curvature radius R_c varies. Here R'_{U_m}s that we obtained in our simulations are consistent with the analytic solution.

Then we conduct a grid independence study. In this case, a capsule moves in a torus flow. First, we fix the Lagrangian grids to 4098, which is fine enough, and change the Eulerian mesh

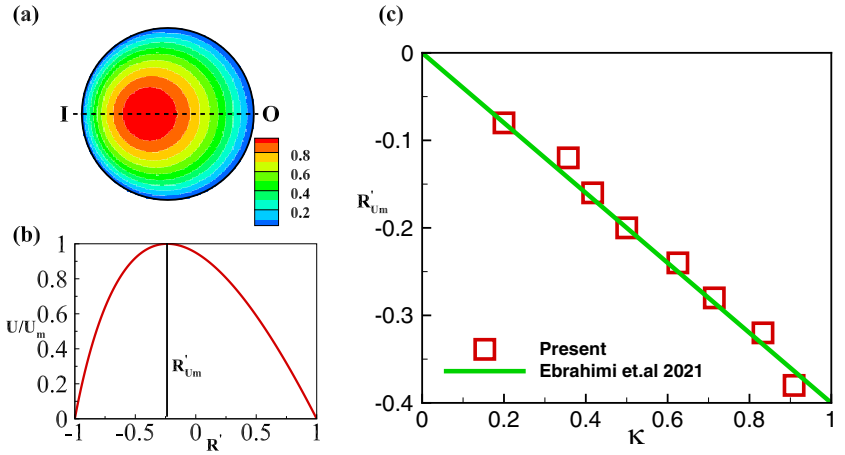

FIG. 3. (a) Azimuthal velocity (scaled by U_m) contours in the case of Re $= 0.05$, $R_c = 3$, $R_t = 2$. The dashed line represents the symmetrical line $Z = 0$. I and O represent the innermost wall (R_i) and outermost wall (R_o) of the vessel, respectively. (b) Distribution of azimuthal velocity along the symmetrical line. The solid line represents the location of U_m. (c) Location of the maximum azimuthal velocity ($R'_{U_{\max}}$) on the symmetrical line in cases of κ : 0.2, 0.357, 0.417, 0.5, 0.625, 0.714, 0.833, 0.9091 at Re $= 0.05$.

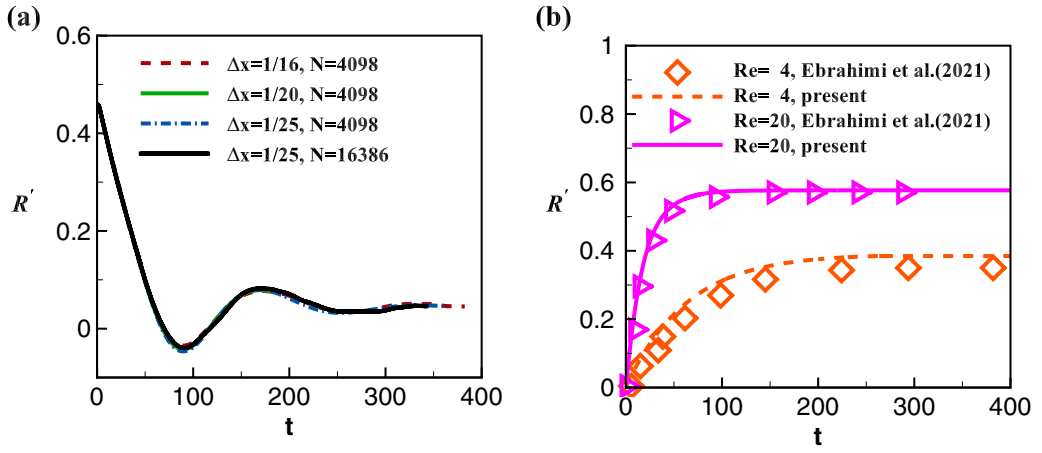

FIG. 4. (a) Radial location of the capsule as a function of time (grid independence study). The key parameters are Re = 10, $Ca = 1.0$, $R_c = 5$, and $R_t = 3$. (b) Results of the cases of Re = 4, 20. The other parameters are $Ca = 1.0$, $R_c = 5$, and $R_t = 4$. Lines represent our results and symbols represent the results of Ref. [40].

size $\Delta x = \frac{1}{16}, \frac{1}{20}, \frac{1}{25}$, and track the radial location of the mass center of the capsule. Figure 4(a) shows that the results with three different Eulerian meshes collapse into a single curve. Then we used more Lagrangian grids to check the grid independence. It is seen from Fig. 4(a) that even more Lagrangian grids ($N = 16386$) are used, the result almost collapses into the identical curve. Therefore Lagrangian grids $N = 4098$ is enough. In our following simulations, the resolution ($\Delta x = \frac{1}{25}, N = 4098$) is adopted.

In addition, using the resolution, we simulated another two cases of Re = 4 and 20. Here a direct comparison [Fig. 4(b)] shows that our results of Re = 4, 20 are consistent with those in Ref. [40].

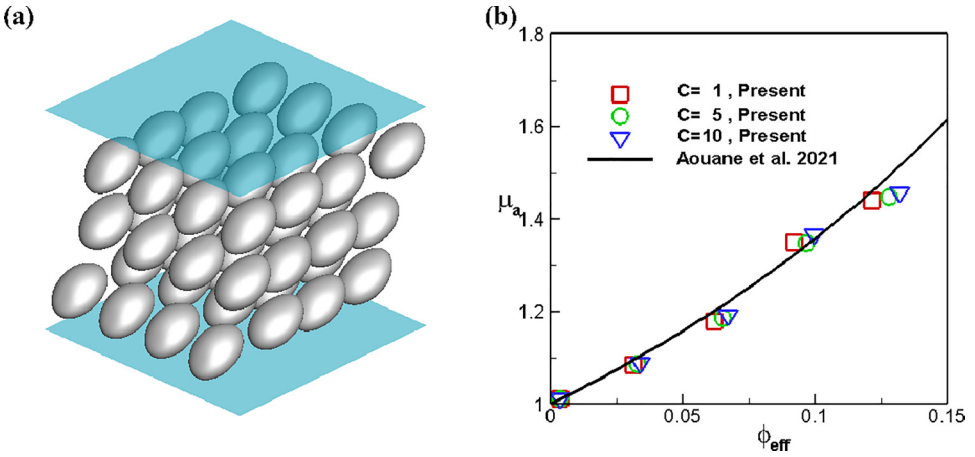

FIG. 5. (a) Typical configuration of capsules ($\phi = 20.11\%, Ca = 0.2$) in the computational domain where three lengths are $10a \times 10a \times 10a$. (b) μ_a as a function of ϕ_{eff} defined in Eq. (3.9) in Aouane *et al.* [61] at Re = 0.01. The mechanical properties of the capsules are $C = 1, 5, 10$, Ca = 0.2, $\phi =$ 0.42%, 3.77%, 7.54%, 11.31%, 15.08%, 20.11%, where the cases of $\phi = 0.42\%$ contain one capsule. The symbols are our results and the black line is the scaling law [Eq. (3.10)] of Aouane *et al.* [61].

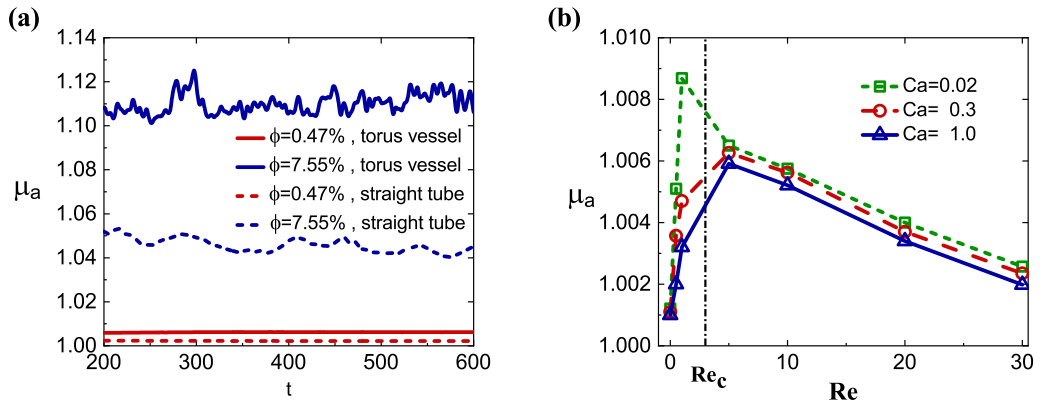

FIG. 6. (a) Evolution of instantaneous μ_a for thecases with different ϕ in torus vessel and straight tube (Re = 5). (b) μ_a as a function of Re for the cases of Ca = 0.02, 0.3, 1.0 at $\phi = 0.47\%$. $\mathrm{Re}_c \approx 3.0$.

At last, we validate the multiple capsule suspensions in a straight channel. Figure 5(a) shows the snapshot of a typical configuration of capsules in shear flow. The apparent viscosity of capsule suspension is compared with that of Aouane *et al.* [61]. From Fig. 5(b), it can be seen that our results are consistent with their scaling law. The code is accurate enough to simulate the flow of suspension in curved tubes.

III. RESULTS AND DISCUSSION

In the following subsections, we simulate the migration of single and multiple capsules in torus vessels and straight tubes. Flow properties of capsule suspensions as functions of Re, κ, and ϕ are presented. Corresponding capsule distributions are also analyzed.

A. Single capsule flow in torus vessels

In this subsection, $R_c = 5$ and $R_t = 3$ are fixed. Since κ is a constant, the intensity of Dean's vortex only depends on fluid inertia Re. We mainly discuss the rheology of the most dilute suspension ($\phi = 0.47\%$), which contains only one single capsule. For the pure fluid flow in the torus vessel without capsules, the volume flux Q_0 under the driven of pressure gradient g is

$$Q_0 = \int_0^{R_t}\int_0^{2\pi} U(R,\theta)RdRd\theta = \left[\frac{1}{2} + \frac{1}{96}k^2 + O(k^3)\right]\frac{g\pi R_t^4}{4\mu_0} = \frac{\lambda}{\mu_0}, \tag{14}$$

where $U(R,\theta)$ is the theoretical azimuthal velocity in the limit of small Re [17]. λ is a constant, which is only a function of g. If the capsule suspension flows in the same torus with pressure gradient g, we have volume flux of the capsule suspension $Q = \frac{\lambda}{\mu}$, where μ is the effective viscosity of the suspension. Then the apparent viscosity is $\mu_a = \frac{\mu}{\mu_0} = \frac{Q_0}{Q}$. Similarly, the apparent viscosity depending on Re is introduced as [33,62]

$$\mu_a = \frac{\mu}{\mu_0} = \frac{Q_l}{Q}, \tag{15}$$

where Q_l and Q are the volume flux of the suspension with and without capsules at the same Reynolds number.

Figure 6(a) shows the instantaneous μ_a in torus vessels and straight tubes under different volume fractions. For the most dilute regime (the red lines), μ_a is almost a constant at the equilibrium state. For the semi dilute regime, the variations of the curves are quite small, which indicates that the equilibrium states are achieved. Here μ_a as a function of Re for different Ca is shown in Fig. 6(b).

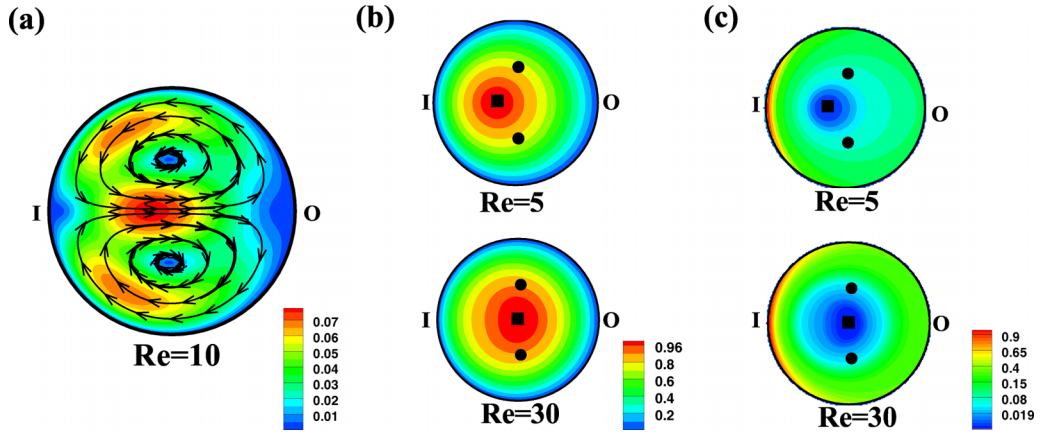

FIG. 7. (a) Contours of secondary velocity $U_s = \sqrt{(u_R^2 + u_Z^2)}$ inside a cross section, where u_R, u_Z are R and Z-component velocities. Streamlines are also shown. (b) Contours of the azimuthal velocity U. It is perpendicular to the paper inward. (c) Contours of the dissipation D which is proportional to the product of the local shear rate $\dot{\gamma}$ and fluid shear stress σ_f, $D \propto \dot{\gamma} \cdot \sigma_f$ [33]. Here U_s, U are scaled by U_m, D is scaled by D_m (maximum of D). Squares represent the locations of U_m in (b) and the locations of the lowest D in (c). The solid dots represent the central locations of the Dean's vortices. I and O represent the inner and outer walls of the vessel.

We can see that μ_a as a function of Re can be divided into two regimes by a critical Reynolds number Re_c [it is defined as the location of the maximum of the curves $\mu_a = f(\mathrm{Re})$], i.e., $\mathrm{Re}_c \approx 3$. For $\mathrm{Re} \leqslant \mathrm{Re}_c$ (Regime I), μ_a increases with Re and is strongly affected by Ca, which is similar to that in a straight tube. However, for $\mathrm{Re} > \mathrm{Re}_c$ (Regime II), μ_a decreases with Re and is not sensitive to Ca. This trend differs from that in a straight tube, where μ_a increases with Re within the parameters we studied [32,33].

We would like to explain the significant difference at Regime II by showing the role of the secondary flow (Dean's vortex). Regime I would also be discussed. The Dean's vortex is shown in Fig. 7(a). There are two counter-rotating vortices on the cross section. The upper and lower vortices rotate counterclockwise and clockwise, respectively. A higher Re leads to a stronger Dean's vortex [19]. Due to Dean's vortices, the location of the maximum azimuthal velocity U_m is shifted. From Figs. 7(b) and 7(c), we can see that in tube flow, the region with larger azimuthal velocity has lower dissipation, which means that if capsules are in the region close to U_m, μ_a would be small. The contours of the azimuthal velocity U are shown in Fig. 7(b), the locations of U_m are labeled by the black squares. It is seen that when Re changes from 5 to 30, the location becomes closer to the centerline of the vessel. On the other hand, the locations of the centers of the Dean's vortex are almost unaffected by Re (see the solid dots). In other words, when Re is larger, the region around the center of the Dean's vortex would be closer to the location of U_m, thus the dissipation of the region becomes lower.

Meanwhile, we would like to discuss the equilibrium lateral locations of the capsules. In typical cases, such as the cases of $\mathrm{Re} = 5$ and 30, capsules all laterally migrate towards the center of Dean's vortex, and at equilibrium states, they stay close to the center [See upper semicircle in Fig. 8(a)]. Hence, as Re increases, at the equilibrium state, the capsule is closer to the low-dissipation region, which is favorable to decrease μ_a. To further illustrate this point, we plot the normalized azimuthal velocities at the equilibrium location of the capsules (U/U_m) [Fig. 8(b)]. For the cases of $\mathrm{Re} > \mathrm{Re}_c$, indeed, U/U_m increases with Re. This is expected because U_m becomes closer to the equilibrium position of the capsule. In addition, the effect of Ca on μ_a is minor since all capsules with different rigidity are trapped by the center of the Dean's vortex.

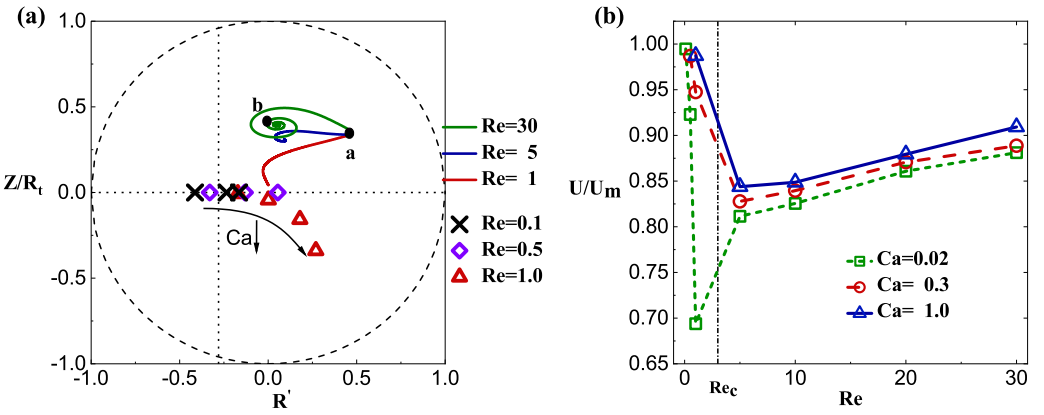

FIG. 8. (a) Trajectories and equilibrium locations of different cases in the cross-section. Upper semicircle: the trajectories of the capsule in the cases of Re $\geqslant 1$ (Re $= 1$, 5 and 30, Ca $= 0.3$). The capsules are all released from the initial position a. Point b denotes the center of Dean's vortex at Re $= 30$. Lower semicircle: equilibrium locations of the capsule in the cases with Re $\leqslant 1$. At the same Re, from left to right, Ca $= 1.0$, 0.3, 0.02, respectively (the case Re $= 1$ and Ca $= 0.1$ is also presented). The intersection of the two dotted lines denotes the location of U_m when Re $\leqslant 1$. Ebrahimi *et al.* [40] also got similar results. (b) The normalized azimuthal velocity U/U_m at the equilibrium position of capsules as a function of Re. In this figure, all cases are calculated with one capsule.

For Re $\leqslant$ Re$_c$, the intensity of Dean's vortex is weak. R'_{U_m} is closer to the inner wall and is not affected by Dean's vortex [see the intersection of the two dotted lines in Fig. 8(a)]. At a low Re, e.g., Re $= 0.1$, the capsules laterally stay almost at the location of U_m and $U/U_m \approx 1$ [see Fig. 8(b)], therefore μ_a is small. As Re increases, they gradually move away from the location of U_m and migrate to a higher-dissipation region [see the equilibrium locations in the lower semicircle of Fig. 8(a)], thus μ_a increases. In addition, at Re $\approx$ Re$_c$, when the capsule is rigid (smaller Ca), the capsule may further move away from the location of U_m [e.g., see the red triangles in Fig. 8(a)]. The behavior would greatly influence μ_a. Then, we performed a quantitative analysis of the relationship between the equilibrium position and Ca at Re $\approx$ Re$_c$, see Fig. 9. Through data fitting, the equilibrium position of capsules as a function of Ca is described quantitatively.

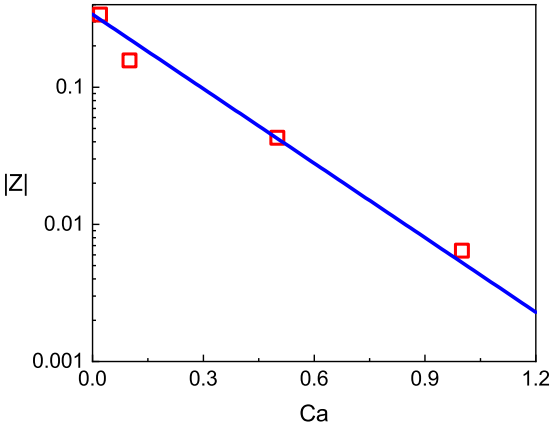

FIG. 9. Equilibrium position in z direction ($|Z|$) as a function of Ca at $\kappa = 0.6$, Re$_c = 3.0$. Red squares are our data, blue line is the exponential fitting formula $|Z| = 0.35e^{-Ca/0.2}$. The y axis is in log scale.

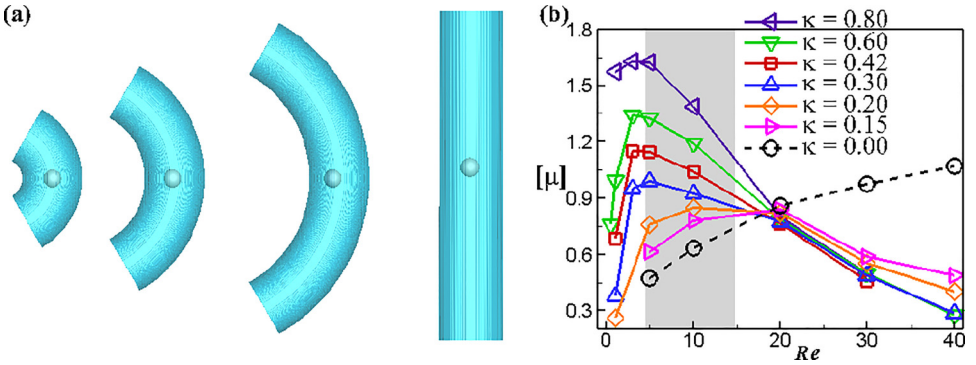

FIG. 10. (a) Configurations of the curved tubes with curvature $\kappa = 0.6, 0.3, 0.2$ and straight tube (from left to right). (b) Intrinsic viscosity as a function of Re in torus vessels with various curvatures and the straight tubes. Each case contains one capsule.

When Ca is small, the equilibrium position is near the Dean's vortices. With the increase of Ca, the capsule would approach the position of maximum azimuthal velocity in an exponential trend. It is noticed that when $\kappa \to 0$ (straight tube), $\mathrm{Re}_c \to \infty$, there is no Dean's vortices and subsequently no $|Z| - \mathrm{Ca}$ curve. However, the exponential relationship between equilibrium radius and Ca is still valid [63].

B. Curvature κ effect

We now turn to the effect of curvature $\kappa = R_t/R_c$ on the viscosity of capsule suspension with limited inertia. We mainly focus on the cases of $\mathrm{Re} > \mathrm{Re}_c$, because in such a regime, μ_a decreases with Re, which differs from common perception. The above subsection shows that in the regime, μ_a does not depend too much on the Ca at $\kappa = 0.6$. This is also the case for all the other configurations but is not shown here, so we keep $\mathrm{Ca} = 0.3$. The fluid properties (ρ and μ_0) and the radius a of capsules are also fixed. Different curvature cases with κ ranging from 0.15 to 0.8 are achieved by changing the curvature radius and tube radius. Segments of the vessels are shown in Fig. 10(a). For comparison, the cases in a straight tube ($\kappa = 0$) are also simulated. To eliminate the effect of ϕ, we define the intrinsic viscosity $[\mu]$ as

$$[\mu] = \frac{\mu - \mu_0}{\mu_0 \phi} = \frac{\mu_a - 1}{\phi}. \tag{16}$$

The intrinsic viscosity $[\mu]$ as a function of Re for different κ is shown in Fig. 10(b). For the cases $\kappa = 0.42, 0.3, 0.2$, overall $[\mu]$ decreases with Re. The variation trend looks similar to that of cases $\kappa = 0.6$, which we discussed above. On the other hand, we also find that the critical Reynolds number Re_c seems associated with κ. For example, $\mathrm{Re}_c \approx 3$ for cases of $\kappa = 0.6$, while $\mathrm{Re}_c \approx 10$ for $\kappa = 0.2$. Then Re_c as a function of κ is plotted in Fig 11(a). Through fitting the data points, we found that Re_c decreases exponentially with κ. When κ approaches 0 (the cases of straight tubes), Re_c approaches infinity. The possible reason is that in a straight tube, there is laminar flow and the viscosity always increases with Re and the transition occurs at $\mathrm{Re} \to \infty$. When κ is large, the Dean's vortices become dominant and μ_a begins to decrease with inertia at a small Re. Therefore Re_c would decrease with κ.

In addition, we can see that the variation trends of torus vessels are opposite to that in a straight tube ($\kappa = 0$). The increasing trend of $[\mu]$ in straight tubes can be explained in the following way. As Re increases, the capsules may migrate away from the centerline of the tube (low dissipation region) to the wall (high dissipation region), which enhances $[\mu]$ [33]. The mechanism is similar to that in the torus vessel at small Re, which is also mentioned in the next subsection.

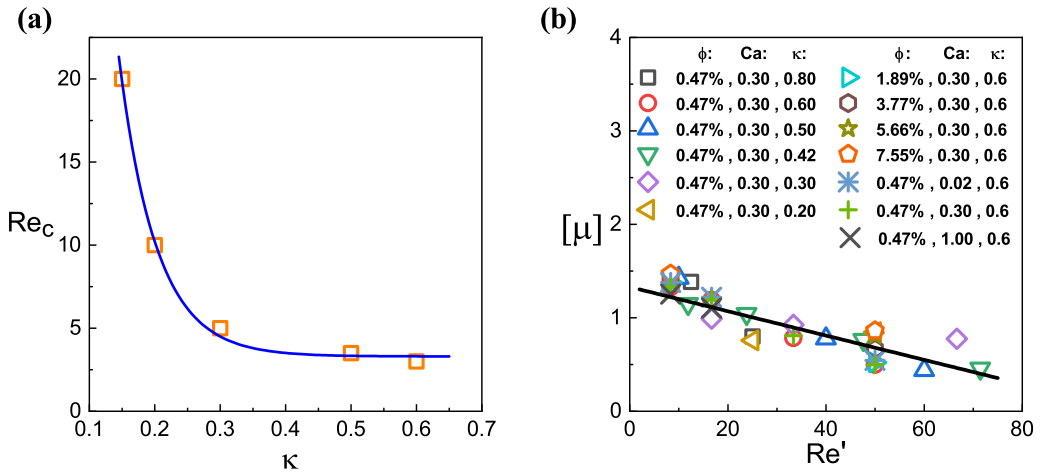

FIG. 11. (a) Transition Reynolds number Re_c as a function of κ. All cases contains one capsule with $\mathrm{Ca} = 0.3$. The orange squares are our results, blue line is the fitting line $\mathrm{Re}_c = 3.30 + 227.45e^{-17.48\kappa}$. (b) Intrisic viscosity $[\mu]$ as a function of Re' at various Ca and ϕ. The line represents a data fitting curve $[\mu] = -0.013\mathrm{Re}' + 1.3$.

Now we focus on the effect of κ on the cases of torus vessels when Re is at the shaded region. It is seen from Fig. 10(b) that $[\mu]$ increases continuously with κ, e.g., $\mathrm{Re} = 5$, the suspension in the vessel with a larger κ appears more viscous. It can be understood as follows. As κ increases, the location of maximum azimuthal velocity R'_{U_m} becomes closer to the inner wall [see Fig. 3(c) and Eq. (13)], but due to the inertia of the capsules, the lateral locations of the capsules change little. In this way, the capsule becomes closer to the high-dissipation region, and $[\mu]$ increases with κ. Here a scaling law for $[\mu]$ in the shaded region of Fig. 10(b) is proposed. If Reynolds number in the region is redefined as $\mathrm{Re}' = \mathrm{Re}/\kappa$, then all the data in the shaded region can almost collapse into a single line $[\mu] = -0.013\mathrm{Re}' + 1.3$ [see Fig. 11(b)]. It is noted that the length that matters for the apparent viscosity is the radius of curvature of the torus R_c instead of R_t.

On the other hand, from Fig. 10(b) we also see that at large Re, when $\kappa > 0.2$, $[\mu]$ is a decreasing function of Re, which is not sensitive to κ. The possible reason is that when Re is large, the strength of Dean's vortices is so strong that the migration of capsules is dominated by them. When $\kappa < 0.2$, as the κ decreases, the strength of Dean's vortices become weak, so the curves decrease slower and slower, see the region outside the shaded one in Fig. 10(b). Here, the cases with very small κ were not performed for the following reasons. First, the cases of smaller κ (large radius of torus), require a large amount of computing resources due to the large computational domain size. Second, our focus is the flow inside significantly curved tubes, where Dean's vortices play an important role. The flow with a small κ (Dean's vortices are very weak) should be close to that of the straight tube ($\kappa = 0$, no Dean's vortices).

C. Flow of semidilute suspensions in torus vessels

In the following, the semidilute regime with multiple capsules are investigated. In this subsection, the size of the torus is fixed, $R_c = 5, R_t = 3$. For the semidilute regime, in addition to the above mechanism, the interaction between capsules may further affect the spatial distribution of capsules as well as the apparent viscosity [64]. The evolution of the instantaneous apparent viscosity μ_a for the case of $\phi = 7.55\%$ is shown in Fig. 6(a). μ_a oscillates around an average value $\bar{\mu}_a$ with a small amplitude ϵ. When $\epsilon < 1\%\bar{\mu}_a$, we suppose the flow reaches an equilibrium state.

Typical snapshots of capsule distributions inside the vessel at equilibrium state for small [left column, (a) and (c)] and large Re [right column, (b) and (d)] are shown in Fig. 12. At small Re,

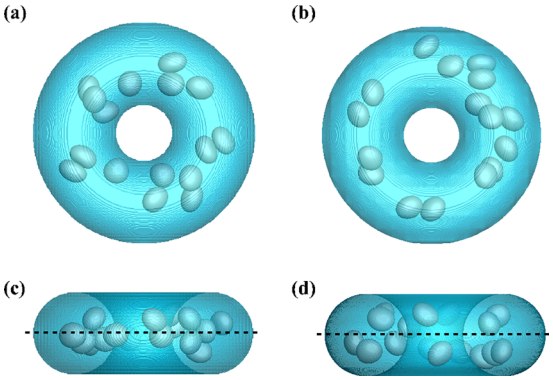

FIG. 12. Typical snapshots of configurations of capsules at equilibrium states ($\phi = 7.55\%$, Ca $= 0.3$). Top view (a), (b) and front view (c), (d) for the cases of Re $= 1.0(a, c)$ and Re $= 30(b, d)$. Dashed lines represent the symmetrical plane.

e.g., Re $= 1$, because the Dean's vortices are weak, overall, capsules are close to the inner wall [see Fig. 12(a)] and concentrated close to the symmetric plane [see Fig. 12(c)]. While at large Reynolds number (Re $= 30$), the Dean's vortex is strong and the capsules tend to migrate laterally to the vortices' centers. The capsules approximately form a two-file structure. The two files seem close to the centers of the upper and lower semicircles [see Figs. 12(b) and 12(d)].

To quantify the distribution of capsules in the torus, we give the temporal and spatial-averaged probability density of capsules, which is defined as

$$P(R, Z) = \frac{1}{2\pi R}\left\langle \int_0^{2\pi} I(R, \theta, Z, t)d\theta \right\rangle, \tag{17}$$

where $I(R, \theta, Z, t)$ is a scalar function and if the lattice node (R, θ, Z) is occupied by the capsules, $I = 1$, otherwise $I = 0$. The symbol $\langle \cdots \rangle$ denotes an averaging over time after reaching an equilibrium state. The time that used to compute the temporal average of the pdf is 400 (dimensionless time) which is long enough. The contours of $P(R, Z)$ at different representative Re are shown in Fig. 13. From Fig. 13(a), we can see that at Re $= 1$, capsules concentrate on the symmetry plane and are close to the inner wall. At Re $= 30$, capsules stay close to the centers of vortices [see Fig. 13(b)], which is similar to the behavior in the single-capsule case. The distribution of capsules is consistent with what we have seen in Fig. 12. Moreover, quantitatively, the temporal and spatial-averaged centroid location of all capsules can be calculated through $(\bar{R}, \bar{Z}) = (\iint P(R, Z)R\, dRdZ, \iint P(R, Z)Z\, dRdZ)$. The temporal and spatial-averaged centroid is labeled as a cross symbol in Fig. 13(a). We can see that the centroid is close to the equilibrium location in the corresponding case of single capsule (solid dots). In addition, a similar phenomenon is also observed in the cases of other volume fractions (not shown). Therefore, it is reasonable to conjecture that the variation of μ_a for semidilute regime is similar to that for the most dilute regime. Figure 14(a) confirms this point. From Fig. 14(a), we can see that at a specific ϕ, μ_a as a function of Re is similar to that of the single-capsule cases in the torus vessels (increasing at small Re, decreasing at large Re).

As a comparison, $P(R, Z)$ in the straight tube is also investigated. The parameters Ca, R_t are the same as those in Sec. III B. Because there is no secondary flow in the straight tube, the distribution of capsules is different from that in the torus vessel. It can be seen that at Re $= 1$, the capsules are concentrated in the center of the tube, see Fig. 13(c). Then at Re $= 30$, the capsules are mainly located inside an annulus between the center and wall [Fig. 13(d)], i.e., inertial focusing phenomenon [65]. The annulus region has a larger shear rate with higher dissipation, which results

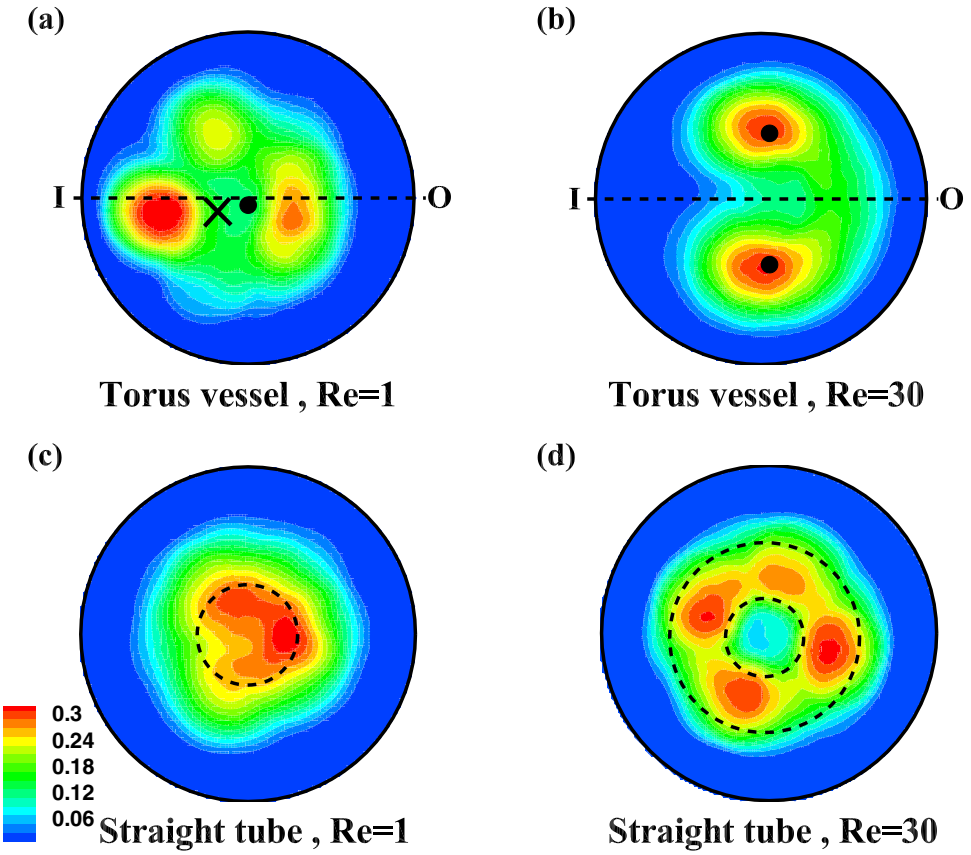

FIG. 13. The temporal and spatial-averaged probability density of capsules P in a cross-section. In all cases $\phi = 11.325\%$. The dashed line in (a) and (b) is the symmetrical line. The dashed circle in (c) and annulus in (d) denote the regions where the capsules are concentrated. The solid dot and cross represent the equilibrium position in the case of a single capsule and the average position of multiple capsules, respectively.

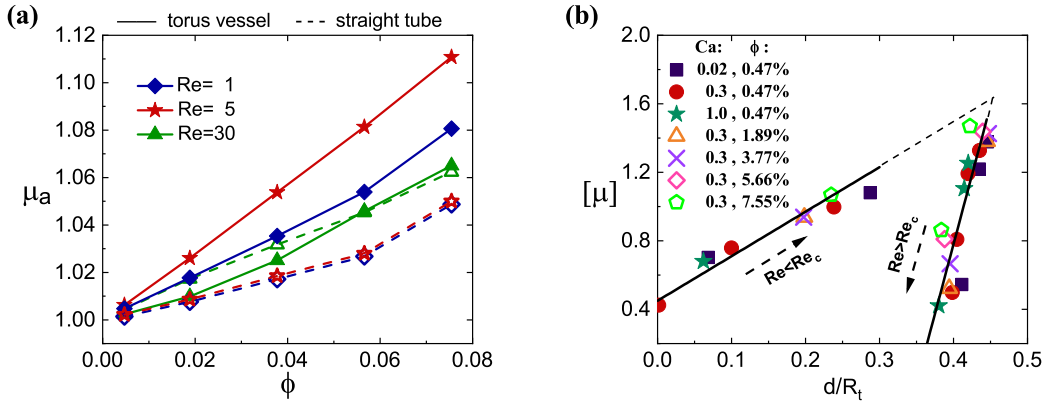

FIG. 14. (a) μ_a as a function of $\phi(0.47\%, 1.89\%, 3.77\%, 5.66\%, 7.55\%)$ in torus vessel (solid lines) and straight tube (dotted lines) at Re $= 1$, 5, 30 and Ca $= 0.3$. (b) Intrinsic viscosity $[\mu]$ as a function of d. The directions of the arrows represent an increase of Re. The dashed line represents a transitional regime Re $\approx$ Re$_c$.

in a larger μ_a [see the dashed lines of Re = 1, 30 in Fig. 14(a)]. Therefore in the straight tube, μ_a generally increases with Re.

In both dilute and semi dilute results, effective viscosity seems directly relevant to the average location of capsules. In the following, we would like to quantify the relationship. The temporal and spatial-averaged distance d between the location of capsules and U_m, is defined as $d = \langle \frac{1}{N}\sum_{i=1}^{N} R_i - R_{U_m} \rangle$, where R_i and R_{U_m} are the positions of the ith capsule and U_m on the cross section, separately. We found that the intrinsic viscosity $[\mu]$ is a piece linear function of d [see Fig. 14(b)]. We can see that $[\mu]$ increases with d slowly when $\mathrm{Re} < \mathrm{Re}_c$, but decreases dramatically with d when $\mathrm{Re} > \mathrm{Re}_c$. Because when $\mathrm{Re} < \mathrm{Re}_c$, roughly capsules stay close to the location of U_m ($d < 0.25$). In the region, the variation of the gradient of U (or viscous dissipation) is small. In other words, although d changes a lot, $[\mu]$ increases gently with d. When $\mathrm{Re} > \mathrm{Re}_c$, capsules stay significantly far away from the location of U_m ($d \approx 0.45$), where the variation of the gradient of U is high. Hence, $[\mu]$ changes dramatically with d.

IV. CONCLUSION

In the present study, the rheology of capsule suspensions in torus vessels is studied by using an immersed-boundary lattice Boltzmann method. We first studied the apparent viscosity μ_a as a function of Re and Ca.When the inertia is small ($\mathrm{Re} < \mathrm{Re}_c$), the capsules tend to stay close to the $Z = 0$ plane. μ_a would increase with Re, because as Re increases, the capsule moves away from the location of U_m and migrates to the high-dissipation region. In addition, μ_a decreases with Ca because the softer capsules (larger Ca) are closer to the location of U_m where the viscous dissipation is low. When the inertia is large ($\mathrm{Re} > \mathrm{Re}_c$), μ_a decreases with Re, which is different from the trend in the straight tube. The Dean's vortices play an important role in the variation trend of μ_a. On one hand, the stronger Dean's vortices at higher Re trap the capsules into their centers. On the other hand, they make the location of U_m closer to their centers. In this way, at higher Re, the capsules become closer to the low-dissipation region, which results in a smaller μ_a. At this regime, μ_a weakly depends on Ca.

Then the effect of curvature κ on the effective viscosity is investigated. When κ is large enough, e.g., $\kappa > 0.2$, the variation trends of torus vessels are opposite to that in a straight tube ($\kappa = 0$). When Re is small, e.g., Re = 5, the suspension in the vessel with a larger κ appears more viscous because the inertia of the capsules makes them stay in the higher-dissipation region as κ increases. A scaling law for the effective viscosity at the small-Re regime is proposed. All data of different κ, Ca, and ϕ in our study support the scaling law. On the other hand, at higher Re, Dean's vortices are dominant, which promotes the capsules' circumferential transportation. Therefore the effective viscosity is a decreasing function of Re, which is not sensitive to κ.

Furthermore, the distributions of multiple capsules in torus vessels and straight tubes are investigated. In torus vessels, at higher ϕ, the capsules tend to concentrate in the symmetrical plane at low Re and tend to be trapped by the Dean's vortices at high Re. Besides, for both the dilute and semidilute regime, the scaling law connecting the effective viscosity and the average location of capsules is proposed. Our data well support the scaling. Our findings may be useful to guide tube design for capsule transportation.

ACKNOWLEDGMENTS

This work is supported by the Natural Science Foundation of China (NSFC), Grant No. 11772326. This project is also supported by the Joint Funds of the National Natural Science Foundation of China (Grant No. U21B2070). In addition, this research is supported by the Supercomputing Center of the USTC.

[1] A. T. W. Cheung, P. C. Y. Chen, E. C. Larkin, P. L. Duong, S. Ramanujam, F. Tablin, and T. Wun, Microvascular abnormalities in sickle cell disease: A computer-assisted intravital microscopy study, Blood **99**, 3999 (2002).
[2] H. C. Han, Twisted blood vessels: symptoms, etiology and biomechanical mechanisms, J. Vasc. Res. **49**, 185 (2012).
[3] P. Blinder, P. Tsai, J. Kaufhold, P. Knutsen, H. Suhl, and D. Kleinfeld, The cortical angiome: An interconnected vascular network with noncolumnar patterns of blood flow, Nat. Neurosci. **16**, 889 (2013).
[4] N. Shahcheraghi, H. Dwyer, A. Cheer, A. Barakat, and T. Rutaganira, Unsteady and three-dimensional simulation of blood flow in the human aortic arch, J. Biomech. Eng. **124**, 378 (2002).
[5] P. Vincent, A. Plata, A. Hunt, P. Weinberg, and S. Sherwin, Blood flow in the rabbit aortic arch and descending thoracic aorta, J. R. Soc. Interface **8**, 1708 (2011).
[6] M. Warkiani, B. Khoo, L. Wu, A. Tay, A. Bhagat, J. Han, and C. Lim, Ultra-fast, label-free isolation of circulating tumor cells from blood using spiral microfluidics, Nat. Protoc. **11**, 134 (2016).
[7] H. Hou, M. Warkiani, B. Khoo, Z. Li, R. Soo, D. Tan, W. Lim, J. Han, A. Bhagat, and C. Lim, Isolation and retrieval of circulating tumor cells using centrifugal forces, Sci. Rep. **3**, 1259 (2013).
[8] M. Bubolz, M. Wille, G. Langer, and U. Werner, The use of dean vortices for crossflow microfiltration: Basic principles and further investigation, Sep. Purif. Technol. **26**, 81 (2002).
[9] S. Kuntaegowdanahalli, A. Bhagat, G. Kumar, and I. Papautsky, Inertial microfluidics for continuous particle separation in spiral microchannels, Lab Chip **9**, 2973 (2009).
[10] A. Bhagat, S. Kuntaegowdanahalli, and I. Papautsky, Enhanced particle filtration in straight microchannels using shear-modulated inertial migration, Phys. Fluids **20**, 101702 (2008).
[11] A. Bhagat, S. Kuntaegowdanahalli, and I. Papautsky, Continuous particle separation in spiral microchannels using dean flows and differential migration, Lab Chip **8**, 1906 (2008).
[12] A. Russom, A. Gupta, S. Nagrath, D. Di Carlo, J. Edd, and M. Toner, Differential inertial focusing of particles in curved low-aspect-ratio microchannels, New J. Phys. **11**, 075025 (2009).
[13] J. M. Martel and M. Toner, Particle focusing in curved microfluidic channels, Sci. Rep. **3**, 3340 (2013).
[14] N. Nivedita and I. Papautsky, Continuous separation of blood cells in spiral microfluidic devices, Biomicrofluidics **7**, 054101 (2013).
[15] N. Nivedita, N. Garg, A. P. Lee, and I. Papautsky, A high throughput microfluidic platform for size-selective enrichment of cell populations in tissue and blood samples, Analyst **142**, 2558 (2017).
[16] D. Di Carlo, D. Irimia, R. Tompkins, and M. Toner, Continuous inertial focusing, ordering, and separation of particles in microchannels, Proc. Natl. Acad. Sci. USA **104**, 18892 (2007).
[17] W. Dean, The stream-line motion of fluid in a curved pipe, London, Edinburgh, Dublin Philos. Mag. J. Sci **5**, 673 (1928).
[18] S. N. Barua, On secondary flow in stationary curved pipes, Q. J. Mech. Appl. Math. **16**, 61 (1963).
[19] L. C. Truesdell Jr and R. J. Adler, Numerical treatment of fully developed laminar flow in helically coiled tubes, AIChE J. **16**, 1010 (1970).
[20] M. Van Dyke, Extended Stokes series: Laminar flow through a loosely coiled pipe, J. Fluid Mech. **86**, 129 (1978).
[21] S. A. Berger, A. L. Talbot, and L. S. Yao, Flow in curved pipes, Annu. Rev. Fluid Mech. **15**, 461 (1983).
[22] K. C. Cheng, R. C. Lin, and J. W. Ou, Fully developed laminar flow in curved rectangular channels, J. Fluid Eng. **98**, 41 (1976).
[23] K. Nandakumar, P. A. J. Mees, and J. H. Masliyah, Multiple, two-dimensional solutions to the Dean problem in curved triangular ducts, Phys. Fluids **5**, 1182 (1993).
[24] C. J. Bolinder, First-and higher-order effects of curvature and torsion on the flow in a helical rectangular duct, J. Fluid Mech. **314**, 113 (1996).
[25] J. Siggers and S. Waters, Steady flows in pipes with finite curvature, Phys. Fluids **17**, 077102 (2005).
[26] R. Chadwick, Slow viscous flow inside a torus–the resistance of small tortuous blood vessels, Q. Appl. Math. **43**, 317 (1985).
[27] N. Tahiri, T. Biben, H. Ez-Zahraouy, A. Benyoussef, and C. Misbah, On the problem of slipper shapes of red blood cells in the microvasculature, Microvasc. Res. **85**, 40 (2013).

[28] Z. Boujja, C. Misbah, H. Ez-Zahraouy, A. Benyoussef, T. John, C. Wagner, and M. Müller, Vesicle dynamics in confined steady and harmonically modulated Poiseuille flows, Phys. Rev. E **98**, 043111 (2018).
[29] Y. Oya and T. Kawakatsu, Onsager's variational principle for the dynamics of a vesicle in a Poiseuille flow, J. Chem. Phys. **148**, 114905 (2018).
[30] B. Kaoui, N. Tahiri, T. Biben, H. Ez-Zahraouy, A. Benyoussef, G. Biros, and C. Misbah, Complexity of vesicle microcirculation, Phys. Rev. E **84**, 041906 (2011).
[31] D. Fedosov, M. Peltomäki, and G. Gompper, Deformation and dynamics of red blood cells in flow through cylindrical microchannels, Soft Matter **10**, 4258 (2014).
[32] H. Feng, H. Huang, and X. Lu, Rheology of capsule suspensions in plane Poiseuille flows, Phys. Fluids **33**, 013302 (2021).
[33] T. Krüger, B. Kaoui, and J. Harting, Interplay of inertia and deformability on rheological properties of a suspension of capsules, J. Fluid Mech. **751**, 725 (2014).
[34] P. Balogh and P. Bagchi, The cell-free layer in simulated microvascular networks, J. Fluid Mech. **864**, 768 (2019).
[35] S. Shin and H. Sung, Inertial migration of an elastic capsule in a Poiseuille flow, Phys. Rev. E **83**, 046321 (2011).
[36] J. Zhou, P. Mukherjee, H. Gao, Q. Luan, and I. Papautsky, Label-free microfluidic sorting of microparticles, APL Bioeng. **3**, 041504 (2019).
[37] T. Ye, N. Phan-Thien, C. Lim, and Y. Li, Red blood cell motion and deformation in a curved microvessel, J. Biomech. **65**, 12 (2017).
[38] T. Ye, N. Phan-Thien, B. Khoo, and Y. Li, Flow patterns and red blood cell dynamics in a U-bend, J. Appl. Phys. **124**, 124701 (2018).
[39] P. Balogh and P. Bagchi, A computational approach to modeling cellular-scale blood flow in complex geometry, J. Comput. Phys. **334**, 280 (2017).
[40] S. Ebrahimi, P. Balogh, and P. Bagchi, Motion of a capsule in a curved tube, J. Fluid Mech. **907**, A28 (2021).
[41] S. Ebrahimi and P. Bagchi, Inertial and non-inertial focusing of a deformable capsule in a curved microchannel, J. Fluid Mech. **929**, A30 (2021).
[42] S. Chien, Shear dependence of effective cell volume as a determinant of blood viscosity, Science **168**, 977 (1970).
[43] S. Chien, S. Usami, R. Dellenback, M. Gregersen, L. Nanninga, and M. Guest, Blood viscosity: influence of erythrocyte aggregation, Science **157**, 829 (1967).
[44] G. Segre and A. Silberberg, Behaviour of macroscopic rigid spheres in Poiseuille flow Part 2. Experimental results and interpretation, J. Fluid Mech. **14**, 136 (1962).
[45] J. P. Matas, J. F. Morris, and E. Guazzelli, Inertial migration of rigid spherical particles in Poiseuille flow, J. Fluid Mech. **515**, 171 (2004).
[46] Y. Morita, T. Itano, and M. Sugihara-Seki, Equilibrium radial positions of neutrally buoyant spherical particles over the circular cross-section in Poiseuille flow, J. Fluid Mech. **813**, 750 (2017).
[47] S. Nakayama, H. Yamashita, T. Yabu, T. Itano, and M. Sugihara-Seki, Three regimes of inertial focusing for spherical particles suspended in circular tube flows, J. Fluid Mech. **871**, 952 (2019).
[48] M. V. Majji and J. F. Morris, Inertial migration of particles in Taylor-Couette flows, Phys. Fluids **30**, 033303 (2018).
[49] Y. Sui, Y.-T. Chew, P. Roy, and H.-T. Low, A hybrid method to study flow-induced deformation of three-dimensional capsules, J. Comput. Phys. **227**, 6351 (2008).
[50] R. Skalak, A. Tozeren, R. Zarda, and S. Chien, Strain energy function of red blood cell membranes, Biophys. J. **13**, 245 (1973).
[51] O. Zhong-Can and W. Helfrich, Bending energy of vesicle membranes: General expressions for the first, second, and third variation of the shape energy and applications to spheres and cylinders, Phys. Rev. A **39**, 5280 (1989).
[52] T. Krüger, H. Kusumaatmaja, A. Kuzmin, O. Shardt, G. Silva, and E. M. Viggen, *The Lattice Boltzmann Method* (Springer, Berlin, 2017), Vol. 10, p. 4.

[53] F. E. Mackay, S. T. Ollila, and C. Denniston, Hydrodynamic forces implemented into LAMMPS through a lattice-Boltzmann fluid, Comput. Phys. Commun. **184**, 2021 (2013).
[54] C. S. Peskin, The immersed boundary method, Acta Numer. **11**, 479 (2002).
[55] Z. Wang, Y. Sui, A. V. Salsac, D. Barthès-Biesel, and W. Wang, Motion of a spherical capsule in branched tube flow with finite inertia, J. Fluid Mech. **806**, 603 (2016).
[56] S. Joung, M. Song, and D. Kim, Synthetic capsule breakup in simple shear flow, Phys. Fluids **32**, 113603 (2020).
[57] C. De Loubens, J. Deschamps, G. Boedec, and M. Leonetti, Stretching of capsules in an elongation flow, a route to constitutive law, J. Fluid Mech. **767**, R3 (2015).
[58] E. Häner, M. Heil, and A. Juel, Deformation and sorting of capsules in a T-junction, J. Fluid Mech. **885**, A4 (2020).
[59] C. de Loubens, J. Deschamps, M. Georgelin, A. Charrier, F. Edwards-Levy, and M. Leonetti, Mechanical characterization of cross-linked serum albumin microcapsules, Soft Matter **10**, 4561 (2014).
[60] X.-Q. Hu, B. Sévénié, A.-V. Salsac, E. Leclerc, and D. Barthès-Biesel, Characterizing the membrane properties of capsules flowing in a square-section microfluidic channel: Effects of the membrane constitutive law, Phys. Rev. E **87**, 063008 (2013).
[61] O. Aouane, A. Scagliarini, and J. Harting, Structure and rheology of suspensions of spherical strain-hardening capsules, J. Fluid Mech. **911**, A11 (2021).
[62] J. Zhang, P. C. Johnson, and A. S. Popel, An immersed boundary lattice Boltzmann approach to simulate deformable liquid capsules and its application to microscopic blood flows, Phys. Biol. **4**, 285 (2007).
[63] N. Takeishi, H. Yamashita, T. Omori, N. Yokoyama, S. Wada, and M. Sugihara-Seki, Inertial migration of red blood cells under a Newtonian fluid in a circular channel, J. Fluid Mech. **952**, A35 (2022).
[64] M. Thiébaud, Z. Shen, J. Harting, and C. Misbah, Prediction of Anomalous Blood Viscosity in Confined Shear Flow, Phys. Rev. Lett. **112**, 238304 (2014).
[65] K. J. Humphry, P. M. Kulkarni, D. A. Weitz, J. F. Morris, and H. A. Stone, Axial and lateral particle ordering in finite Reynolds number channel flows, Phys. Fluids **22**, 081703 (2010).